AIAA JOURNAL
Vol. 35, No. 6, June 1997

Numerical Wave Propagation and Steady-State Solutions: Soft Wall and Outer Boundary Conditions

K. Mazaheri* and P. L. Roe†
University of Michigan, Ann Arbor, Michigan 48105

In the numerical solution of the external steady inviscid flows (governed by the Euler equations) around a solid body, error waves can be damped or eliminated from the nonsteady solution process at three different places: the inner boundary, the computational field, and the outer boundary. Techniques for doing this leading to faster convergence to a steady state are presented. Visualization techniques, which help us to understand, design, and develop new ideas, are also presented. Error waves are damped at the inner boundary by using a soft wall condition, instead of the common rigid wall boundary condition. This boundary condition is analyzed, its application in one and two space dimensions are developed, gains of up to 50% in running time are presented, and reasons for not helping in the presence of shock waves are discussed. Finally to accelerate the convergence via the outer boundary, it is shown that in many cases the outgoing waves are not, as commonly assumed, normal to the boundary. Then it is shown why and how the slowing down of the waves near the outer boundary can accelerate the convergence. Some new boundary models are introduced, which take into account the angle of incidence to minimize the reflections.

I. Introduction

A. Euler Equations

In two space dimensions, the time-dependent Euler equations can be written as

$$\boldsymbol{u}_t + \mathcal{A}\boldsymbol{u}_x + \mathcal{B}\boldsymbol{u}_y = 0 \tag{1}$$

Simple wave solutions could be written in the form

$$\boldsymbol{u} = \boldsymbol{u}(\boldsymbol{x}\cos\theta + \boldsymbol{y}\sin\theta - \lambda t)$$

which, indeed, shows solutions that are constant on straight lines in the xy plane, moving with speed λ in the direction of its unit normal $\boldsymbol{n} = (\cos\theta, \sin\theta)$. The characteristic surfaces are moving with corresponding speeds of

$$\lambda_{4,1} = u\cos\theta + v\sin\theta \pm a \qquad \lambda_{2,3} = u\cos\theta + v\sin\theta$$

Note that in numerical solution of the Euler equations (and many other fluid dynamics equations), the errors and the residuals of the conserved variables are convected, dispersed, and dissipated like a scalar quantity. For example, for the evolution of ρ_t in the one-dimensional Euler equations, one may write

$$(\rho_t)_t - [(\rho u^2 + p)_x]_x = 0$$

and similar results could be found for two space dimensions. Therefore, it is natural to study the behavior of these waves to develop any technique that involves them, particularly in convergence acceleration studies. Techniques are developed to allow experimental study of the residual waves. Some results of these experiments follow.

B. Experimental Study of Residual Waves

Video films are made, which show how the solution evolves. Results reported in this section are for a simple first-order upwind scheme using local time stepping on a rather coarse grid (see Fig. 1), to find the solution of the Euler equations around a NACA0012 airfoil at $M = 0.63$ and $\alpha = 2$ deg. In fact, this code is used because it behaves rather simply and predictably, but enough tests are made with other schemes and finer grids to have some confidence in the general conclusions. Figure 2 shows the residual history for both single and double precision calculations.

Stills from one such video are shown in Figs. 3a–3d, which show contours of area-weighted residuals (cell area $\times|\rho_t|$). The area weighting is used as a way of emphasizing the far-field behavior. The video reveals very clearly that the path to convergence follows a simple, well-defined, repetitive pattern that begins almost immediately.

Given an initial solution equal everywhere to the freestream (plus the circulation due to a vortex), acoustic disturbances can be seen to propagate both upstream and downstream. The waves going downstream are mainly expansive, while those going upstream are compressive waves focusing into a shock wave. Because of local time stepping, this shock moves faster as it moves out into the coarser mesh and becomes almost planar. This is what would be predicted by applying Huyghen's principle and allowing for local propagation speeds.

The average residual remains almost constant while the forward shock is moving outward; as the shock reaches the boundary, the residual falls rapidly. However, shortly afterward, a fresh set of waves originates (apparently spontaneously, but almost certainly triggered by reflected waves returning from the boundary) and the cycle repeats, although at a generally reduced amplitude. For the first six cycles, occupying the first 1000 iterations, there are minor variations, but after this each cycle repeats the previous one very faithfully. After the first cycle, almost all of the largest (weighted) residuals appear in the front-half of the flow. A perfect correlation is maintained between the timing of these waves and the beating in a conventional residual history (as in Fig. 2).

Figure 3a shows the residual pattern after 1235 explicit time steps. The regions labeled (★), (★★), and (★★★) could be tracked in time to gain insight into the convergence process. In Fig. 3a, the region (★) is leaving the computational domain. A new forward-moving wave is being generated near the trailing edge creating fresh high residuals. Meanwhile, the previous wave has not yet completely left the domain. This is the moment of fastest convergence. After this, the residual falls rapidly as the last of the forward-going waves escapes.

By 1410 time steps (Fig. 3d), the pattern of Fig. 3a has been reestablished, with region (★★) taking the place of the original region (★), and region (★★★) taking the place of the original region (★★).

If the calculation is made in single precision, then after about 2000 iterations, the residuals are close to machine zero, and the residual pattern seen in the video degenerates into random noise. However, if the calculation is performed in double-precision arithmetic, then the pattern continues and becomes increasingly regular. The residual history of both cases are shown in Fig. 2a.

The explanation of this particular sequence is a little mysterious. One may conjecture that the seemingly spontaneous emission of

Received Feb. 21, 1995; revision received Feb. 3, 1997; accepted for publication Feb. 4, 1997.

*Research Assistant, Department of Aerospace Engineering; currently Assistant Professor, Aerospace Engineering Group, Sharif University of Technology, Tehran 11365-9567, Iran. Member AIAA.

†Professor, Aerospace Engineering.

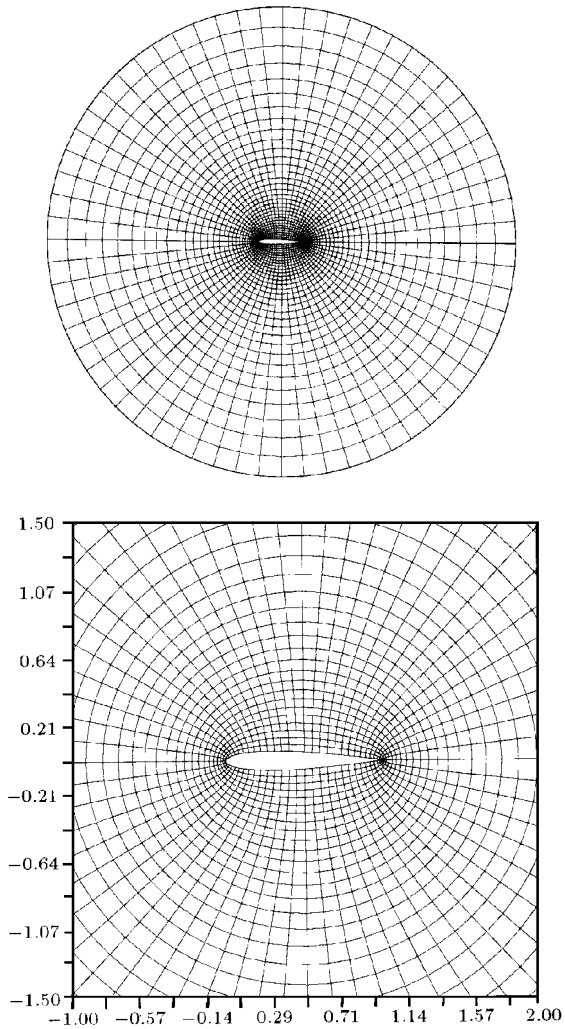

Fig. 1 Grid used in computation, 64 × 32, is generated using Laplace equation; outer boundary is a circle with radius five times the chord, centered in the middle of it.

waves from near the trailing edge is due to focusing of reflected waves that are themselves too weak to show up in the residual pattern (as displayed). To confirm this, calculations are made in which the shape of the wave front is explicitly tracked (see the Appendix). It is shown there that for a single simple wave front, started from the surface of the airfoil body, all reflections arrive on the airfoil body at almost the same time.

C. Conclusions

All of these observations are convincing evidence that acoustic waves are responsible for an important part of the convergence process. An additional observation, suggesting that acoustic behavior is almost completely dominant, comes from correlating the pressure and density residuals. For any purely acoustic disturbance, one should find that

$$p_t = a^2 \rho_t \tag{2}$$

In fact, one finds that this equation holds to within 1% on average over the flowfield.

After one basic cycle, i.e., the time required for the residual wave to traverse once the computational flowfield (forward and backward, from airfoil to the outer boundary, and reverse), the amplitude of the residual waves can be expected to be reduced by a factor of something like

$$R = R_f R_o R_i \tag{3}$$

where R_f is the attenuation due to numerical dissipation (whether by accident or design) as the waves traverse the flow twice, R_o is the attenuation when the wave reflects from the outer boundary, and R_i is the attenuation when the wave reflects from the inner solid boundary. It is believed that these facts should provoke a complete

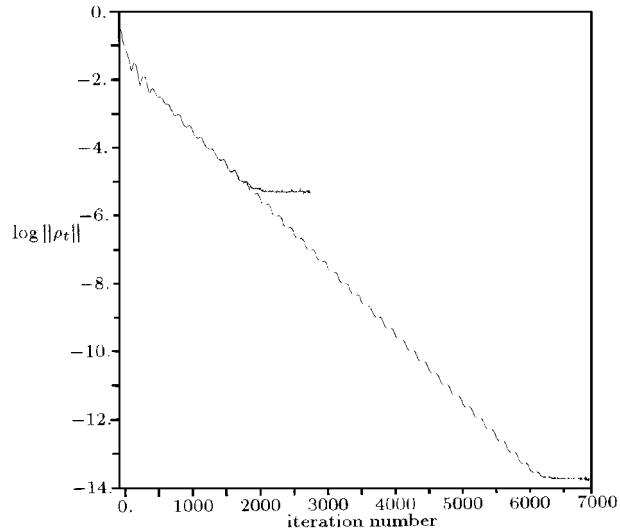

Fig. 2 Residual history for single- and double-precision computations: ——, single precision and – – –, double precision.

reexamination of boundary procedures and numerical schemes. In Sec. II, work is conducted that is aimed at preventing the regeneration of residuals by attenuating these continued reflections at the other end of their journey, that is, at the solid surface. In Sec. IV, techniques are shown to decrease R_o.

II. Soft Boundary Conditions

At first sight, a solid inner boundary implies $R_i = 1$, and we are not aware of any previous attempt to change this. However, it is decided here to experiment with replacing the boundary condition

$$u_n = 0 \tag{4}$$

by the more general boundary condition

$$\frac{\partial u_n}{\partial t} + \frac{u_n}{\tau} = \frac{\mu}{\rho a}\frac{\partial p}{\partial t} \tag{5}$$

which should coincide with Eq. (4) in the steady limit. Here, τ and μ are parameters that are chosen with the intention of minimizing reflected disturbances. It can be shown that the new boundary condition [Eq. (5)] acts as a massless spring-damper system (Fig. 4), with driving force per unit length p, stiffness coefficient $k = 1/\mu\tau$, and damping coefficient $c = 1/\mu$.

A. One-Dimensional Analysis

To choose τ and μ, the model problem of one-dimensional acoustics is considered, governed by

$$u_t + \rho_0^{-1} p_x = 0 \qquad p_t + \rho_0 a_0^2 u_x = 0 \tag{6}$$

in the quarter-plane $t > 0$ and $x < 0$. Everything is nondimensionalized by ρ_0, a_0, and a length scale l, equal to the distance between left and right boundaries. At $t = 0$, initial conditions are specified as $u = 0$, $p(x, 0) = P(x)$, and Eq. (5) is taken to be the boundary condition on $x = 0$.

The solution (Fig. 5) takes the form of the incident waves plus a set of reflected waves in the region $x + a_0 t > 0$. Both pressure and velocity on the wall vary sinusoidally with the same frequency ω. Introducing the strength of returning waves $s_r(0, t) = |p - \rho_0 a_0 u| = [p(0, t) - p_0] - u(0, t)$ and the strength of the incoming waves as $s_i = |p + \rho_0 a_0 u| = \bar{p}$, one can use $S = s_r/s_i$ as a measure of ratio of amplitude of the reflected waves vs the incident waves. Then, assuming a sinusoidal initial condition $P(x) = p_0 + \bar{p}\sin[(\omega/a)x]$, the magnitude of the steady-state part of this reflection coefficient can be found to be

$$|S| = \sqrt{\frac{1 + (\omega\tau)^2(1-\mu)^2}{1 + (\omega\tau)^2(1+\mu)^2}} \tag{7}$$

For high-frequency waves ($\omega\tau \gg 1$),

$$|S| = |(1-\mu)/(1+\mu)|$$

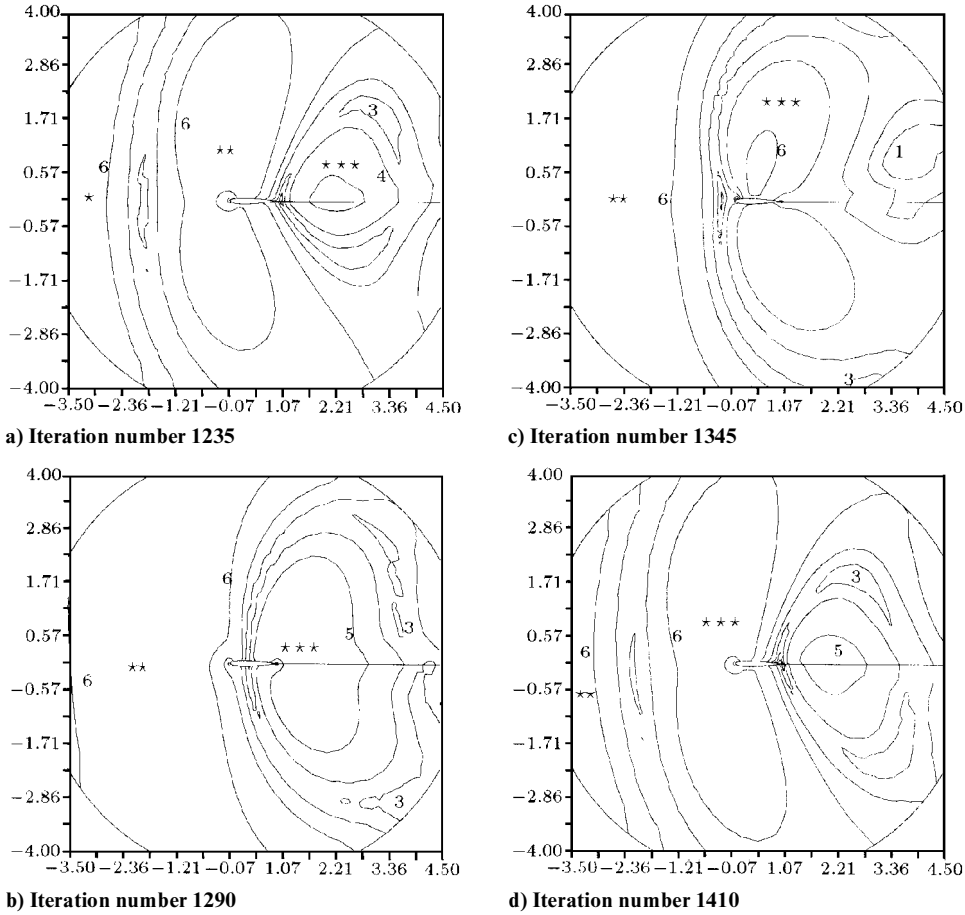

Fig. 3 Residual contours, for two-dimensional flow around NACA0012, $M = 0.63$, $\alpha = 2$ using first-order Roe's upwind scheme with the contours in logarithmic scale: 1, _2.4; 2, _2.0; 3, _1.6; 4, _1.2; 5, _0.8; 6, _0.4; and 7, 0.0.

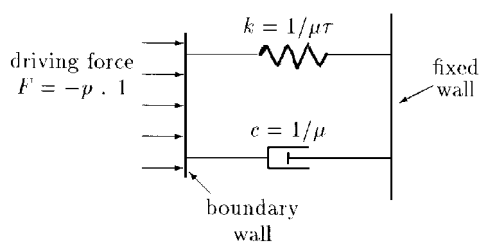

Fig. 4 Massless spring-damper system.

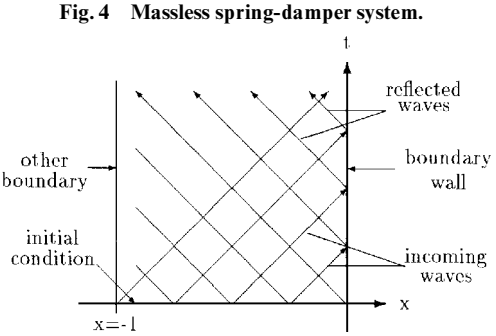

Fig. 5 Sketch of the model.

Numerical values for $|S|$ [Eq. (7)] are shown in Fig. 6; the horizontal axis shows $\omega\tau$, and the vertical axis is μ. One can see that the reflection is minimized (for any ω) by taking $\mu = 1.0$ and τ large compared to ω. Note that u is then proportional to the strength of the outgoing acoustic waves.

To check that this result was not confined to the special case of sinusoidal incident waves, the analysis is repeated for a Gaussian incident wave

$$p(x\ .0) = p_0 + \bar{p}\exp\left[\_\beta(x + \tfrac{1}{2})^2\right] \tag{8}$$

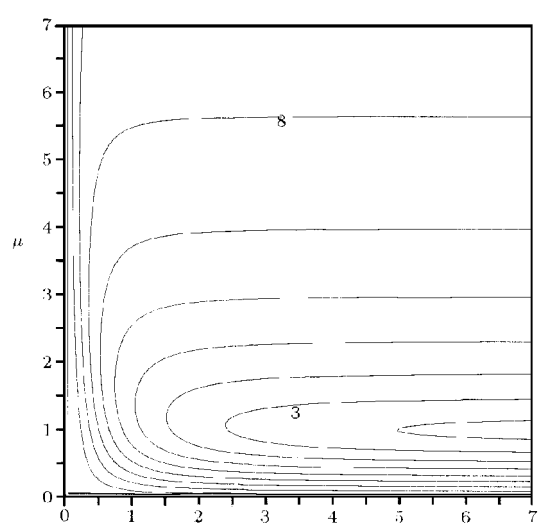

Fig. 6 Strength of reflected waves for an initial sinusoidal pressure distribution; strength levels: 1, 0.0; 2, 0.1; 3, 0.2; 4, 0.3; 5, 0.4; 6, 0.5; 7, 0.6; 8, 0.7; 9, 0.8; and 10, 0.9.

A similar analysis to that results in

$$S(t) = \exp\left[\_\beta\left(\_t + \frac{1}{2}\right)^2\right] \_ 4\beta\mu\prime e^{-t/\tau\prime}$$

$$\times \int_0^t \left(\frac{1}{2} - \zeta\right) \exp\left[\_\beta\left(\_\zeta + \frac{1}{2}\right)^2 + \frac{\zeta}{\tau\prime}\right] \mathrm{d}\zeta$$

$$= F(\mu\prime, \beta, \tau\prime; t)$$

where $\tau\prime = \tau(1 + \mu)$ and $\mu\prime = \mu/(1 + \mu)$.

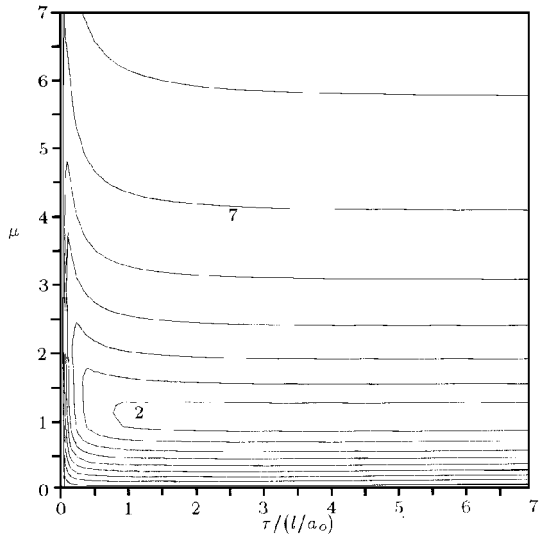

Fig. 7 Strength of reflected waves for an initial Gaussian pressure distribution; strength levels: 1, 0.0; 2, 0.1; 3, 0.2; 4, 0.3; 5, 0.4; 6, 0.5; 7, 0.6; 8, 0.7; 9, 0.8; and 10, 0.9.

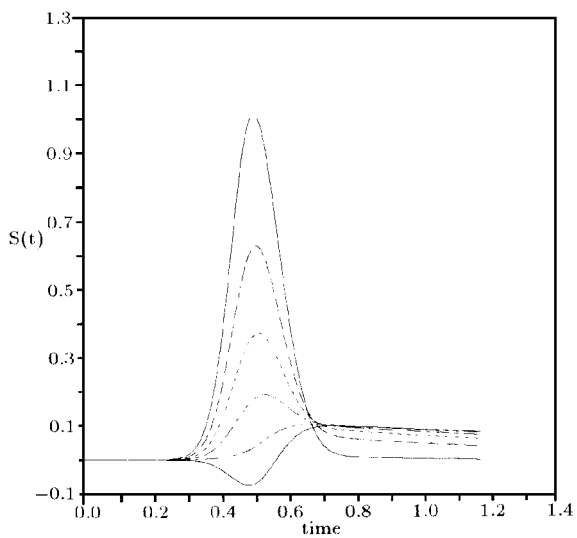

Fig. 8 Strength of reflected waves for different values of μ here $\tau/\Delta t$ = 100; strength levels: ——, 0; – – –, 0.25; - - - -, 0.50; – – – –, 0.75; – – – –, 1.00; and ——, 1.25.

The steady-state part of this is plotted in Fig. 7. Again the preferred combination is $\mu = 1$ and τ large with respect to ω However, if τ its made too large, then after the impact of the wave is past, the wall velocity returns only slowly to zero. In fact, the parameter τ is loosely bounded by two considerations. One of these is that τ must not be much less than a typical timestep; otherwise one may have difficulty in modeling the equation. On the other hand, τ should not be greater than the round-trip time for a wave to cross the domain, for then the next returning wave will not encounter the proper boundary.

Also, when it comes to apply these boundary conditions to a two-dimensional example, one realizes that the preceding analysis, although correct, is not the most helpful. For an input wave of essentially finite duration, not only the peak amplitude of the returning wave is significant, but also the amplitude at the moment when the incident wave ceases, and the returning wave begins to decay freely. This determines how quickly the wall returns to its unperturbed position.

Figure 8 shows the results of a series of (exact) calculations in one-dimensional analysis, to be used to determine the optimum value of μ for a one-dimensional problem. The field is the same as earlier, with the initial Gaussian disturbance. Different lines in Fig. 8 show the amplitude of the reflected wave for different values of μ and constant $\tau/\Delta t = 100$. The upper solid line shows the amplitude of the reflected waves (at $x = 0$) for a rigid wall ($\mu = 0$). Note that as μ is increased, the amplitude of the tail also increases, although the peak amplitude has also been decreased. The minimum peak amplitude can be found for $\mu = 1$ (last dotted line in the figure), as mentioned before. This one-dimensional analysis seems to indicate a value of μ roughly equal to 0.5 providing a reasonable compromise between these requirements, and this was also about the value that gave best convergence in the two-dimensional experiments. With more cells in the mesh, local time stepping needs more iterations to send the wave on a round trip, so that one can tolerate a slower return to rigidity. It is found that on meshes with greater numbers of mesh points, the optimal value of μ is greater than 0.5, but the precise value does not seem to be very critical.

B. Discretization

Normally, when a cell interface coincides with a solid boundary, it is only necessary to provide some formula for the pressure on that interface because all other components of the flux will vanish. For the first-order code, the wall pressure is simply set equal to the pressure in the first cell. Here, it is allowed that there may be flow through such an interface and so need to have a complete description of all variables. One would also like to construct the discretization so that steady solutions are unaffected by the changed boundary condition (BC).

These inner BCs are easier to discretize than nonreflecting outer BCs for two reasons. The first is that waves really do arrive, to a good approximation, normal to the boundary (see the Appendix) and, indeed, this approximation improves as finer grids are used. The second is that the mesh is finer near the body than near the outer boundary.

The scheme that was used combined a simple discretization of Eq. (5) with two characteristic equations, one for the incoming acoustic wave (in a one-dimensional approximation) and one for the particle path. The x–t stencil used is shown in Fig. 9. Point 1 represents the state in the center of the cell next to the wall at the end of the last timestep. Point R represents the point at which the boundary flux was evaluated in the previous timestep and S the similar point for the current timestep (or the current stage in multistage calculations). Point B is the extrapolation of the current solution to the wall. Note that δ_1 and δ_2 are nondimensionalized, and $\delta_1 + \delta_2 = 1.0$, but δ_t^k has dimension of time (the superscript k stands for the stage of the computation). In single-stage calculations, $\delta_1 = \delta_2 = 0.5$ and $\delta_t^1 = \Delta t$.

There will be three equations:

$$u_t + \frac{u}{\tau} = \frac{\mu}{\rho a} p_t$$

$$\mathrm{d}p - a^2\,\mathrm{d}\rho = 0 \qquad \text{on} \qquad \frac{\mathrm{d}x}{\mathrm{d}t} = u$$

$$\mathrm{d}p + \rho a\,\mathrm{d}u = 0 \qquad \text{on} \qquad \frac{\mathrm{d}x}{\mathrm{d}t} = u + a$$

Then one will have

$$\frac{u_S - u_R}{\delta t^k} + \frac{u_S + u_R}{2\tau} = \frac{\mu}{\rho_R a_R}\frac{p_S - p_R}{\delta t^k}$$

$$p_S - a_R^2\rho_S = p_R - a_R^2\rho_R - \frac{\delta t^k}{\Delta x/2}u_R$$

$$\times\left\{[(\delta_2 p_S + \delta_1 p_R) - p_1] - a_R^2[(\delta_2\rho_S + \delta_1\rho_R) - p_1]\right\} \qquad (9)$$

$$p_S + \rho_R a_R u_S = p_R + \rho_R a_R u_R - \frac{\delta t^k}{\Delta x/2}(u_R + a_R)$$

$$\times\left\{[(\delta_2 p_S + \delta_1 p_R) - p_1] + \rho_R a_R[(\delta_2 u_S + \delta_1 u_R) - u_1]\right\}$$

Here linear interpolation is used, e.g., $u_B = \delta_2 u_S + \delta_1 u_R$. These can be solved directly to find conditions at S. For multistage calculations, there are many possible ways to apply this soft wall BC. One can see that all reasonable choices produce similar results.[1]

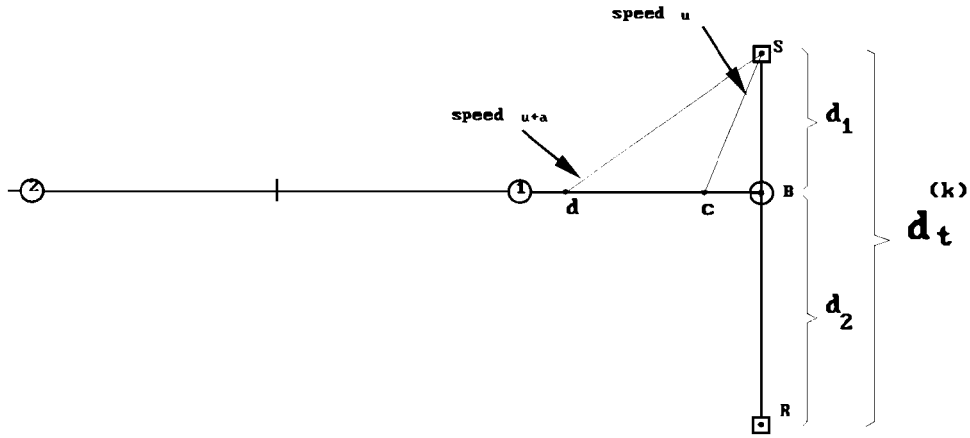

Fig. 9 Sketch of the generalized stencil used in the boundary discretization.

At convergence, when conditions at S and R are the same, one can see from these equations that

$$u_S = 0 \qquad p_S - a_R^2 \rho_S = p_1 - a_R^2 \rho_1 \tag{10}$$

$$p_S + \rho_R a_R u_S = p_1 + \rho_R a_R u_1 \tag{11}$$

Although the last of these might be a reasonable BC (to first order) it does not coincide with the condition $p_S = p_1$ used in the regular code. Therefore, u_1 is replaced by u_R in the last term of Eq. (9). No stability problems was observed to be created, and then identical converged solutions were obtained from both the soft wall and solid wall version of the code.

The order of accuracy required in practice is often more than one. One may use standard practice to make the soft wall BC second-order accurate. Similar corrections as described can be made to make the steady-state solution the same as second-order rigid-wall BC, which assumes (for uniform grid)

$$p_R = \tfrac{3}{2} p_1 - \tfrac{1}{2} p_2$$

Extensive numerical experiments show that these corrections only affect the lift coefficient history, but anything else in the solution evolution is almost unchanged. Experiment also shows that for our grid (Fig. 1) assumption of uniform grid does not change the solution evolution significantly.

C. Numerical Experiments

To check how this works at the discrete level, two sets of experiments were accomplished. In the first experiment, the suggested boundary conditions were used for the one-dimensional linearized Euler equations [Eqs. (6)] in the same domain as in the preceding section, for a Gaussian initial disturbance. As expected, even for a high-amplitude wave, for all different values of τ and μ, results in complete consistency with the earlier exact analytical calculations were obtained (i.e., the reflected amplitude, and also, the optimal values for τ and μ agree with the theory) (Fig. 10).

Next, the full Euler equations were solved in the same domain. These experiments were set to test the boundary procedure developed in Sec. II.B. Many experiments were executed for low- and high-amplitude initial pressure distribution. For the low-amplitude waves, for nearly all values of τ and μ, behavior similar to the exact solution was observed. For high-amplitude initial waves, as expected, qualitative agreement was seen (see Figs. 10 and 11). Because the problem is now strongly nonlinear, the theoretical prediction is only qualitative. However, it is found that the trends with respect to τ and μ were preserved; in particular, the optimum values were nearly unaltered.

Figure 10 compares $S(t)$ for a Gaussian initial condition for a high-amplitude wave ($\bar{p}/p_0 = 0.8$) obtained in the following ways. First, using new boundary conditions with $\mu = 0.3$, $\tau/\Delta t_{\text{cell}} = 80$, and 1) numerical experiment for linearized equations, 2) numerical experiment for full nonlinear equations, and 3) exact calculations

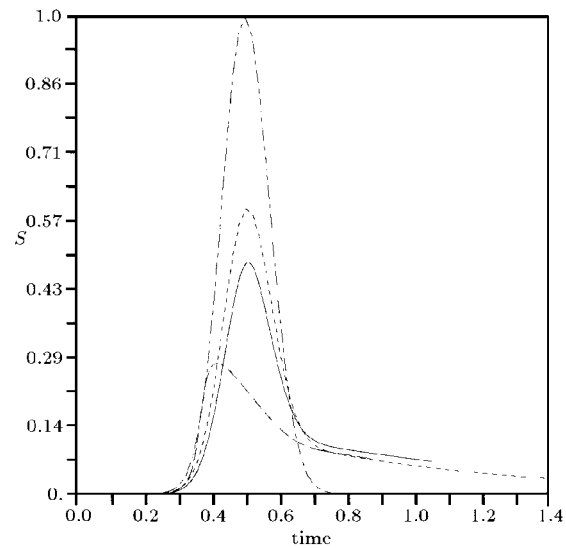

Fig. 10 Comparison of $S(t)$ for Gaussian initial disturbance with $\bar{p}/p_0 = 0.8$: ——, linear code; – – –, nonlinear code; - - - -, linear exact calculation; and – – – –, rigid wall.

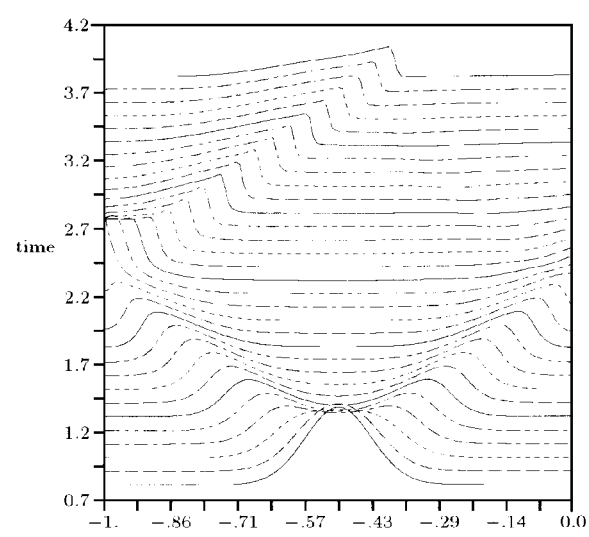

Fig. 11 Pressure distribution evolution; the right-hand-side BC is the new BC with $\tau/\Delta t_{\text{cell}} = 300$ and $\mu = 1.0$, and the left-hand side is a rigid wall; note that $\bar{p}/p_0 = 0.8$.

for linearized equations (see Sec. II.A). Second, exact calculations were obtained for linearized equations with a rigid wall.

Experiment shows that using nonoptimal choices of parameters allows partial reflection of waves from the right-hand boundary. In Fig. 11 the near-optimal choices $\tau/\Delta t_{\text{cell}} = 300$ and $\mu = 1.0$ are used, then it is seen that this high-amplitude initial disturbance is very strongly damped. Actually, in applications reported subsequently, mostly weak disturbances need to be treated, inasmuch as here one is only concerned about residual waves, which are very weak after the first stages of the calculation.

To sum up, these one-dimensional experiences show that a soft wall BC can be implemented and can greatly reduce wave reflections while ultimately achieving the same steady state. In the next section, these results will be applied to two-dimensional flow.

III. Two-Dimensional Applications

To generalize this to two space dimensional calculation, one would decompose the velocity vector at the wall to two normal and parallel components, and then use the preceding equations for the normal component, assuming that the parallel component will not be affected by this boundary procedure.

The testing ground for these ideas in two dimensions was the same airfoil code used in Sec. I.B (Fig. 1, with $M = 0.63$ and $\alpha = 2$ deg). The only modification made was to replace the simple rigid wall boundary conditions with Eq. (5). Again, the code is a first-order upwind scheme, using Roe's flux-difference splitting method.[2] The parameters used were $\mu = 0.5$ and $\tau/\Delta t_{\text{cell}} = 100$. The value of μ and $\tau/\Delta t_{\text{cell}}$ were found experimentally, although with hindsight the arguments in Sec. II.A could have been used to justify the choice of μ. A simple argument to motivate the choice of $\tau/\Delta t_{\text{cell}}$ is as follows.

Under local time stepping, with Courant number ν, the number of iterations required for a wave to pass downstream from the trailing edge to the outer boundary, or from the outer boundary to the leading edge, will be roughly N_R/ν, where N_R is the number of cells in the radial direction. To travel in the reverse direction will take $(N_R/\nu)[(1+M)/(1-M)]$ iterations, giving a total of $2N_R/[\nu(1-M)]$. To ensure that the boundary perturbation dies away before the next wave returns, one may require

$$\exp\left[\frac{-2N_R(\Delta t_{\text{cell}}/\tau)}{\nu(1-M)}\right] \ll 1$$

or, e.g.,

$$\frac{2N_R\Delta t_{\text{cell}}}{\nu(1-M)\tau} > 2$$

where

$$\frac{\tau}{\Delta t_{\text{cell}}} < \frac{N_R}{\nu(1-M)}$$

A typical result is shown in Fig. 12. The evolution divides into three phases. In the first phase, no advantage is seen for the soft boundary. In the second phase, beginning with the first arrival of returning waves at the airfoil, the residual for the soft boundary is substantially reduced, and the oscillations are much less marked. Visualization of the residuals (see Sec. I), however, shows that the recurrent wave pattern is still present. Experiment shows that the lift coefficient is slower to build up with the soft boundary, but converges more steadily. After about 1400 iterations, the residual for the soft boundary has been reduced by about six orders of magnitude, which might be enough to justify halting the code. With the rigid boundary, the same reduction is not achieved until about 2300 iterations, which is a saving of about 40%. The extra computations required for the boundary procedure is negligible with respect to the overall computations. Similar results are achieved with any change of parameters in the range $0.7 > \mu > 0.4$ and $300 > \tau/\Delta t_{\text{cell}} > 50$.

After this time, a third phase sets in, during which the soft boundary again shows only slight advantage. This seems to be because its work is essentially over. Video film of this phase shows that the soft wall calculation no longer features any noticeable wave propagation. Instead, a rather static pattern of residuals appears on the screen and is rather slowly damped. The flux through the wall also

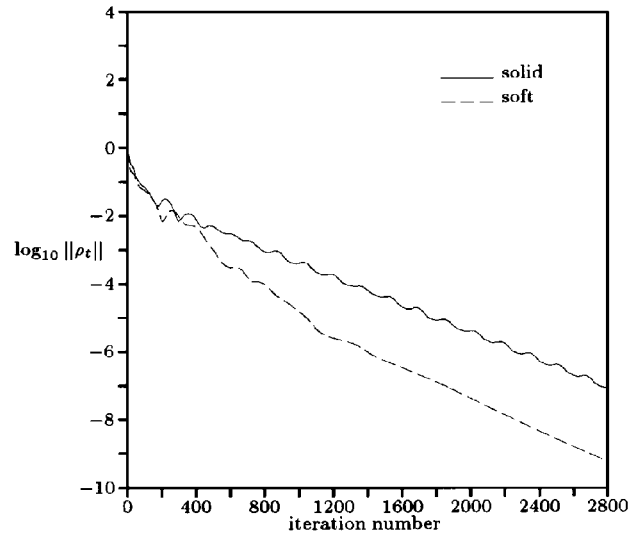

Fig. 12 Comparison of residual history for solid and soft inner BC: ——, solid and – – –, soft.

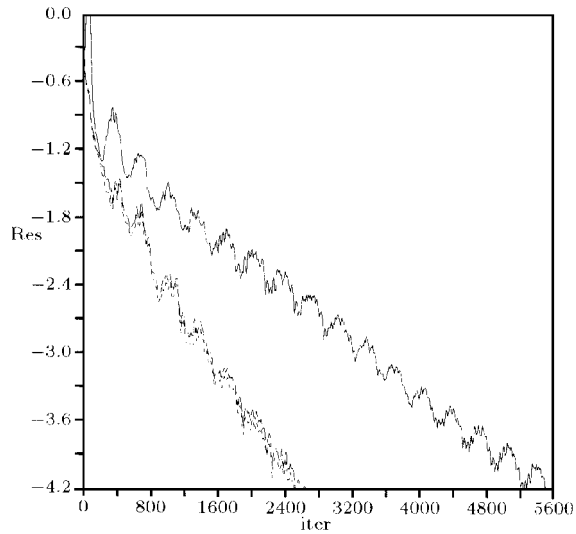

Fig. 13 Effect of soft wall BC in second-order upwind computations on residual history; $\tau = 100\Delta t$, $\mu = 0.7$, single stage: ——, rigid; – – –, without correction; and - - - -, with correction.

continues to diminish. This last phase of convergence is not seen in single-precision calculations because machine accuracy is reached first.

Extensive experiments show that multistage soft wall results are completely similar to single-stage calculations. However, performance of soft wall BC in second-order calculations is different and is illustrated in Fig. 13. The solid line shows the original soft wall, whereas the other two curves show the residual history for soft wall BC, respectively, without and with the correction (to get rigid wall steady-state results). Unlike the first-order calculations, in second order, soft wall increases the convergence rate for both low and high values of residual. In fact, this can be seen similarly in application of soft wall BC in central differencing codes (like Ref. 3). Of course, this is not surprising, because in this case more high frequency waves are moving around, and they can be effectively damped by the soft wall. Experiment shows that, similar to one-dimensional case explained in Sec. II.B, the mentioned correction does not affect the convergence history, and it changes the steady-state solution to the standard second-order BC results. The reasoning for this result is as before.

To see the dependence of the soft wall BC on the Mach number, a series of numerical experiments are done on a NACA0012 airfoil, with 2 deg of angle of attack. All calculations are performed via first-order single-grid single-stage upwind. One may expect to see

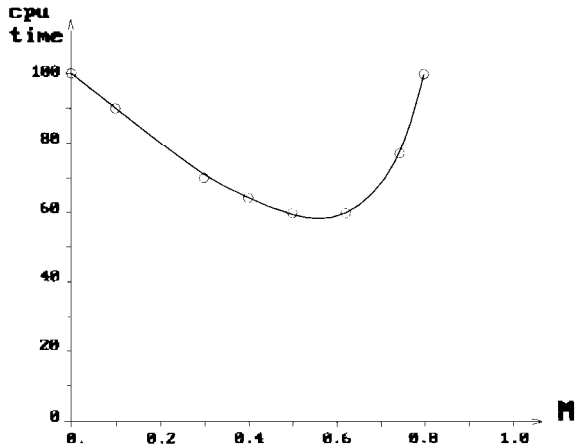

a) Mach numbers

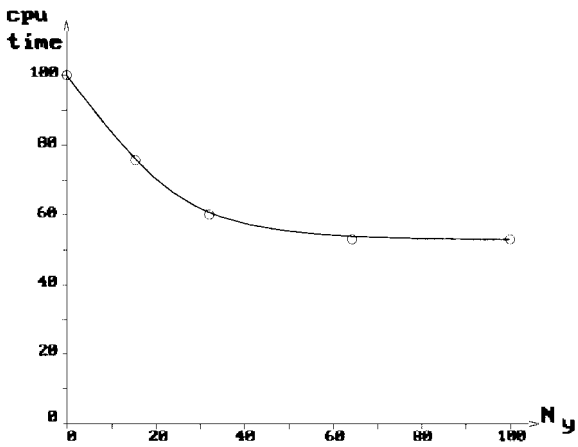

b) Grid sizes

Fig. 14 Performance of soft wall at different Mach numbers and grid sizes.

similar results for other cases. The grid for this calculation is 32×64 O type, shown in Fig. 1. Value of τ is computed according to earlier guidelines in this section, and $\mu = 0.5$. The effect of soft wall on convergence rate in this case is shown in Fig. 14a. The x axis shows different values of the Mach number, whereas the y axis shows how long the soft wall BC calculation takes, when the corresponding calculation for the rigid wall is assumed to take 100 unit times. This figure shows that whereas the soft wall works weakly for low Mach numbers and adversely for transonic flow, it works fairly well for moderate subsonic flows.

It is not so hard to explain this behavior. The main feature of the flow, which is exploited by soft wall, is the repetitive forward movement of waves. In very low Mach numbers, the reflections from the outer boundary are very weak because waves arrive fairly normal to the outer boundary (see the Appendix). Therefore, the focusing effect (also explained in the Appendix) will be less dominant in the convergence process, and soft wall BC will lose most of its advantage. In transonic flow, as video films reveal, the formed shock waves on the surface of the airfoil absorb all forward-going waves, which are moving near the airfoil. This results in losing the advantage of soft wall, which was absorbing the waves, and keeping its disadvantages, which is lagging the convergence process due to allowance of flow through the airfoil surface. This results in a slower convergence process. Indeed, when shock appears on the airfoil, the best BC for the wall will be the classical rigid wall condition.

The test case for the effect of the grid size study is the same airfoil problem, with O grid of size $2N_y \times N_y$, where N_y is the number of cells in a direction normal to the airfoil. The flow is subsonic $M = 0.63$ with 2-deg angle of attack. A value of τ is assumed according to guidelines earlier in Sec. 3, and $\mu = 0.5$. Figure 14b shows the dependence of the soft wall BC on grid size. The x axis shows N_y. As in Fig. 14a, the y axis shows the consumed CPU time for the soft wall BC, when the corresponding rigid wall calculation is assumed to take 100 time units. As one may expect, for a finer grid, it is possible to apply this BC more accurately and hope for better performance. More important than this is that in fine mesh one allows for more wave modes to exist, which delay the convergence, therefore, a mechanism to remove these waves should be more favorable to rapid convergence. Also note that these waves return at longer intervals, and the wall has time to set before they arrive. Gains of 50% are seen.

IV. Absorbing BC

The problem arises from the domain of many physical problems, governed by hyperbolic partial differential equations (PDEs), are not naturally bounded, but in their numerical simulation there is almost no choice other than truncating the domain. In most numerical problems of this kind, this artificial boundary and the conditions to be satisfied there, to simulate the effects of the whole absent universe, is of great importance in stability and convergence. The wavelike solutions near infinity need a BC to simulate the radiation of energy out of the computational field. Any inaccuracy to do this will cause spurious reflected waves to be returned back to the computational field. It is generally believed that one major factor delaying the convergence of computational fluid dynamics (CFD) solutions to a steady state is the time taken for these reflected waves to travel repeatedly between the solid surface and the outer boundary. Figure 2 shows a familiar oscillating path toward convergence that is plausibly explained by such behavior. Therefore, better (radiative) BCs will not only increase the accuracy but also will accelerate the convergence.

Much effort, therefore, has been devoted to the design of absorbing or nonreflective BCs to be applied at the outer boundary. These are, however, almost always based on some intuitive assumption about the manner in which the waves travel back and forth. For example, the assumption is made in Ref. 3 that the waves travel normal to the boundary and that a one-dimensional analysis is adequate (i.e., the tangential derivatives are ignored). Engquist and Majda[4] developed an hierarchy of approximate nonreflecting BCs for multidimensional problems. The first-order member of this hierarchy is the one-dimensional BC in boundary normal direction, and higher-order conditions will also have reflections for nonnormal angle of incidence. In Refs. 5 and 6, acoustic waves originating at the solid surface are considered, so that it is assumed that the angle at which the waves cross the boundary is known.

One may believe that the first of these assumptions is almost never true (see the Appendix). The second may be true if a time-accurate path is followed but makes no allowance for any form of preconditioning, such as local time stepping. In this section, first it will be shown how important assumption of normal incidence is. Then we will try to develop new BCs, which are appropriate for certain incidence or reflection angles and are not restricted to the assumption of normal incidence. Then the question will remain how accurately one can find the dominant angle of incidence of the residual waves near the outer boundary.

A. Slowing Down the Waves

In all works presented in preceding sections, the far-field boundary conditions were one-dimensional characteristic-based equation, neglecting the tangential derivatives on the boundary.

It is difficult to write a reliable rotated Riemann solver, or rotated BC, which is appropriate for oblique waves. But, it is fairly easy, at least in a local time stepping calculation, to force the outgoing waves to hit the far-field boundary at a right angle. The naive way to do this is to try to change the shape of the outer boundary so that it is parallel to the outgoing wave front. This has several practical grid generation complications, especially if a time-accurate solution is sought. Another way is to slow down the waves as they approach the outer boundary. This will have a twofold effect. First, this will slow down the waves, which certainly will decelerate the convergence. The other effect is that because the speed of the waves decreases as they approach the outer boundary the waves will arrive almost normal to the outer boundary, similar to ocean waves arrive almost

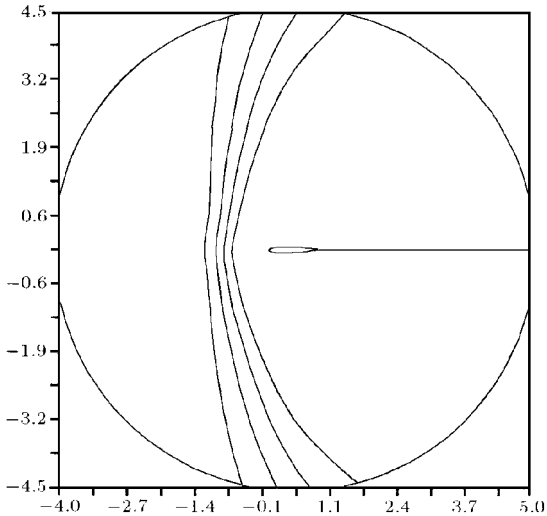

a) Original code

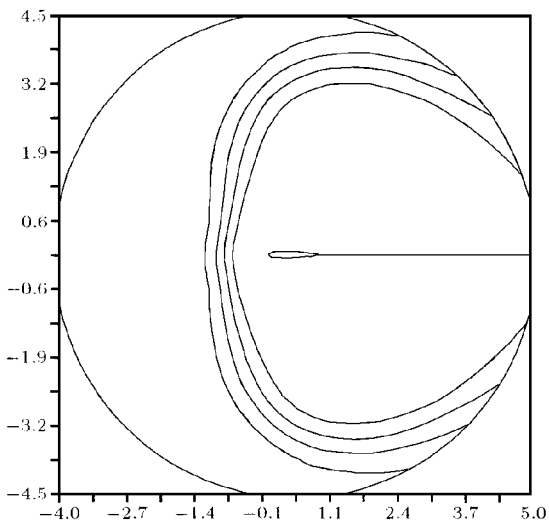

b) Code with slowing down (note how the inicidence angle is different from the normal angle)

Fig. 15 Outgoing waves at time step 100.

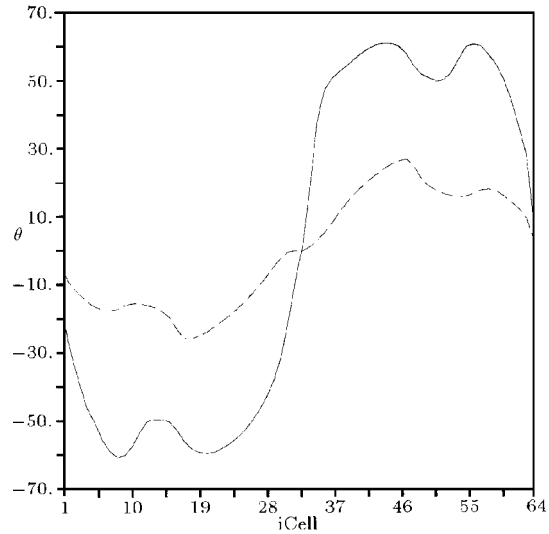

Fig. 16 Effect of slow down on the incidence angle: ——, original and – – –, with slow down.

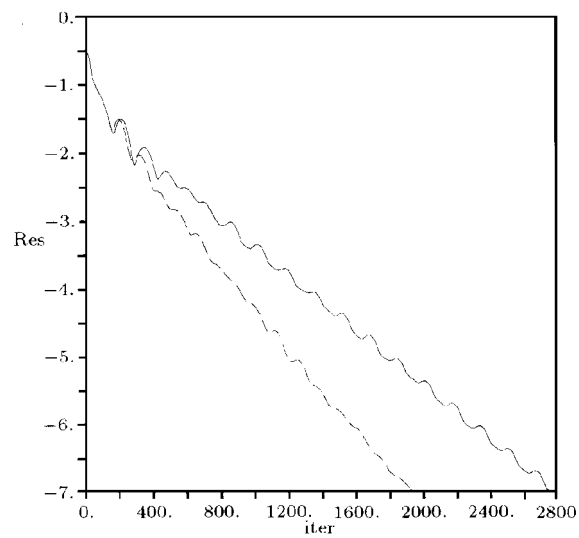

Fig. 17 Effect of slow down on the residual history; ——, original and – – –, with slow down.

normal to the shore. Therefore, reflections are less, and hopefully convergence will be accelerated. Thus, compromise is called for, and the overall results may be optimized by restricting the slow-down to the extent that makes the waves only almost normal to the boundary.

The numerical implementation of this idea is trivial: one just needs to multiply the local timestep with a coefficient, which decreases as one approaches to the outer boundary. One way to do this is

$$\Delta t_{\text{new}} = \left[1 + \alpha e^{-\beta R^2}\right]^{-1} \Delta t_{\text{org}}$$

where R is some measure of the distance from the far-field boundary and α and β are two positive tunable constants. High values of β cause less cells to be affected, and so it is preferable to have high values of β. For the O type grid used in this experiment, with a circular far-field boundary of radius five chords, centered at point (0.5, 0.0) (see Fig. 1), one has

$$R = 5 - \sqrt{(x - 0.5)^2 + y^2}$$

Experimentally one finds that for our subsonic airfoil problem, the results are almost optimum for $\alpha = 5$ and $\beta = 1$.

Figures 15a and 15b show the level contours for the ϕ_1 outgoing waves (for details, see the Appendix). Note how the outgoing waves are deformed in the latter figure, to have a more normal incidence to the boundary. This is shown in Fig. 16, where the incidence angle is compared in these two cases. Here the x axis is the cell number, counted clockwise starting from the cell on the boundary corresponding to the tail of the airfoil, and the y axis is the angle between normal of the wave front and normal of the far-field boundary. Finally, Fig. 17 shows how this simple computation can accelerate the convergence. It is also obvious that the residual history is now more smooth, which may represent a better far-field boundary condition and less reflections at the outer boundary.

B. Reflection Angle

Although the incidence angle may be visualized numerically, the reflection angle has no chance to be displayed by easy numerical manipulation, because it is usually much weaker than the incident wave, and there is no easy way to filter it out from the observed combination. One may erroneously assume that the reflection is just the mirror image of the incident wave. As the following calculation shows, this is not true in general for a moving medium. Figure 18 shows part of the far-field boundary, where the flow is assumed to be horizontal with Mach number M. Here β is the angle between the boundary normal and the flow direction.

Consider a part of the outgoing wave front $\overline{AB}$, at time t. At time $t + \Delta t$ this front gets to point $A\prime$, and $\overline{A\prime B\prime}$ is part of the reflected wave front. Here α is the angle between the incident wave normal n_1 and the boundary normal n_o, and $\alpha\prime$ is the unknown angle between the reflection normal n_2 and the boundary normal n_o. One

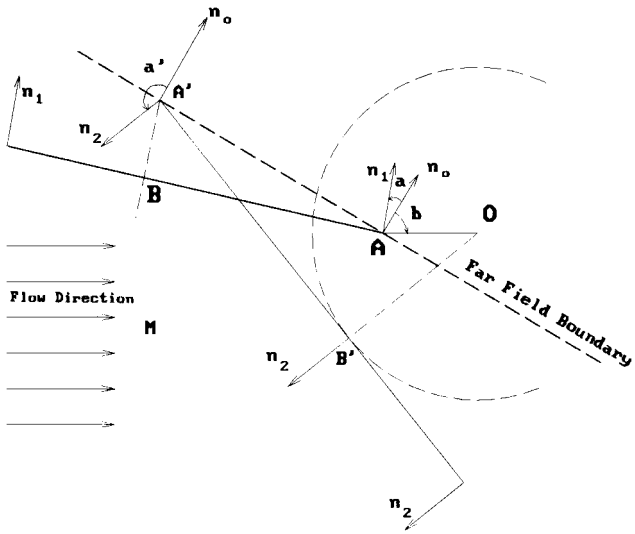

Fig. 18 Sketch of a part of the far-field boundary and the incident and reflected waves.

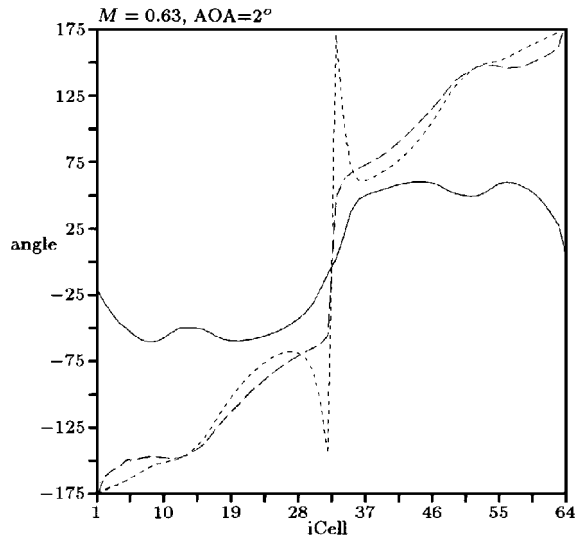

Fig. 19 Comparison of the exact and computed values of the reflection angles; ——, incidence α; – – –, computed $\alpha\prime$; and - - - -, calculated $\alpha\prime$.

may assume $-(\pi/2) < \alpha < \pi/2$, and consider counterclockwise direction (with respect to n_o) to be positive.

If we define

$$M_n = M\cos\beta, \qquad \eta = \tan^{-1}\left(\frac{M_n \sin\alpha}{1 + M_n \cos\alpha}\right)$$

and

$$\delta = \sin^{-1}\left\{\frac{\sin\alpha}{\sqrt{1 + M_n^2 + 2M_n\cos\alpha}}\right\}$$

one can show that $\sin(\alpha\prime - \eta) = \sin\delta$, therefore,

$$\alpha\prime = \begin{cases}\delta + \eta \\ \pi - \delta + \eta\end{cases} \tag{12}$$

There are two possible values for δ; here the smaller absolute value is chosen (i.e., we assume $|\delta| \leq \pi/2$), the other one will be constructed by variations of $\alpha\prime$. Geometrically it is obvious that there are two solutions for $\alpha\prime$, one of them is not relevant and can be shown to be equal to α (with the preceding choice of δ). Let us assume $|\alpha| \leq \pi/2$; of course, both α and $\alpha\prime$ are in the interval $[-\pi, \pi]$. Because $\alpha\prime$ should correspond to an incoming wave, from the possible two choices we will chose the one whose absolute value is larger. Geometrically, the condition for existence of one relevant solution is $|M_n| \leq 1$; otherwise in Fig. 18 no valid tangent to the circle can be made, which means that no reflection happens. Equation (12) shows that except for the case that there is no normal flow, i.e., $M_n = 0$, the reflection angle is different from the mirror image of the incident angle.

Figure 19 shows a comparison between the values of the reflection angles computed from Eq. (12) and the computed values based on the techniques explained in the Appendix. The figure only shows the incidence and reflection angles for the first set of waves arrived at the boundary, due to a perturbation on the airfoil surface at initial time. The x axis is the cell number, as in Fig. 16. The y axis shows the incidence angles (the solid line) measured from results generated by the eikonal equation (Appendix), the reflection angle measured from the same results, and finally the value calculated by applying Eq. (12) to the measured incidence angle. The difference between last two curves is due to inaccuracy in eikonal calculations, especially near the point on the boundary corresponding to the leading edge of the airfoil. As discussed in the Appendix, due to interaction of primary waves in this region, details at this region are probably missing in the current calculations. In fact, as one may see in Fig. 20, these interactions do not allow reflections to be visible. Also note that, contrary to our expectations, for some part of the boundary, $|\alpha\prime|$ calculated by Eq. (12) is less than $\pi/2$. By these results, one can more clearly see the physics of the residual waves reflecting from the outer boundary, the matter claimed in Sec. I. To apply these ideas in tailoring absorbing BCs, two models are suggested here.

C. Designing Absorbing Boundary Conditions

We present some ideas that may be used in better application of absorbing BCs. To have the strength of reflected waves equal to zero, if $u^{\star\star}$ is the component of the velocity in the direction of the reflected wave normal, one requires

$$\mathrm{d}p + \rho a\,\mathrm{d}u^{\star\star} = 0 \tag{13}$$

to be satisfied everywhere. Let us denote the velocity component in the direction of outgoing waves by $u^{\star}$. According to what we showed in Sec. I.C, this is very close to the direction of the outgoing acoustic waves θ_{ac_o}. One also needs three other equations to find all of the unknowns on the boundary. For the inflow portion, one may write

$$\begin{gathered}(p + \rho a u^{\star\star})_B^{k+1} = (p + \rho a u^{\star\star})_B^k \\ (p + \rho a u^{\star})_B = (p + \rho a u^{\star})_N \\ u_B^t = u_{N+1}^t \qquad (p/\rho^\gamma)_B = (p/\rho^\gamma)_{N+1}\end{gathered} \tag{14}$$

Here, subscript N is the last cell, $N+1$ the far-field boundary ghost cell, and B the boundary face. The superscript t is for boundary tangential direction, and k is the time step. For the outflow portion, similar equations could be derived. At this point, numerical results do not show any preference for this method.

Another idea is to decompose the time derivative of the state variables as

$$\boldsymbol{u}_t = \sum_{i}^{4} \alpha_i \boldsymbol{r}_i$$

where $\boldsymbol{r}_i$ are the right eigenvectors of $(\cos\theta A + \sin\theta B)$ for unsteady Euler equations. Therefore, one finds

$$\begin{pmatrix}\rho \\ u \\ v \\ p\end{pmatrix}_t = \alpha_{\mathrm{ac}_i}\begin{pmatrix}\rho \\ -a\cos\theta_{\mathrm{ac}_i} \\ -a\sin\theta_{\mathrm{ac}_i} \\ \rho a^2\end{pmatrix} + \alpha_{\mathrm{ac}_o}\begin{pmatrix}\rho \\ a\cos\theta_{\mathrm{ac}_o} \\ a\sin\theta_{\mathrm{ac}_o} \\ \rho a^2\end{pmatrix}$$

$$+ \alpha_{\mathrm{en}}\begin{pmatrix}1 \\ 0 \\ 0 \\ 0\end{pmatrix} + \alpha_{\mathrm{sh}}\begin{pmatrix}0 \\ -\sin\theta_{\mathrm{sh}} \\ \cos\theta_{\mathrm{sh}} \\ 0\end{pmatrix}$$

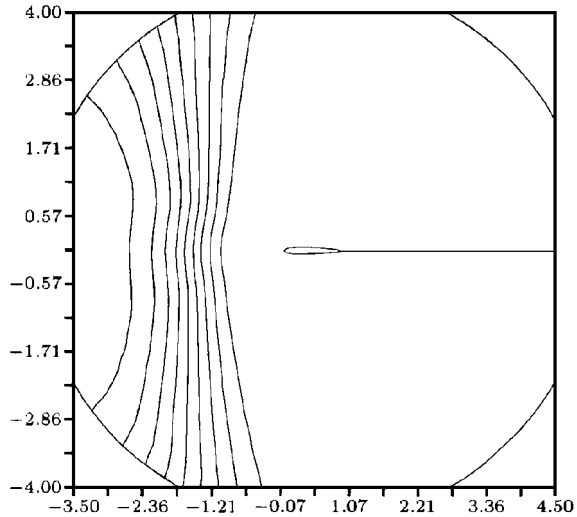

a) ϕ_1

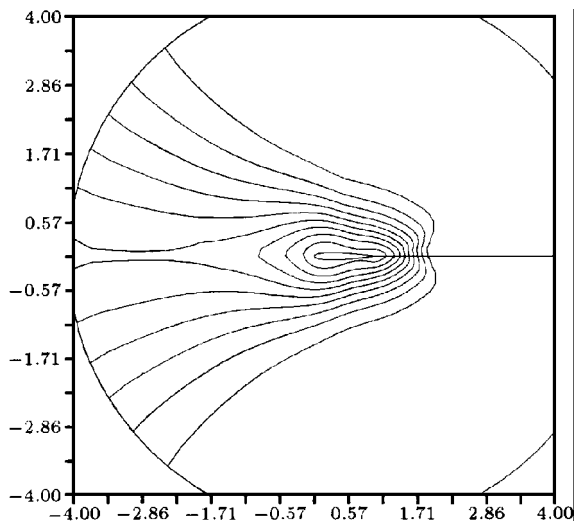

b) ϕ_2

Fig. 20 Contours at iteration number 120.

Here, subscript ac_i is incoming acoustic wave, ac_o outgoing acoustic wave, en entropy, and sh shear wave. Solving for $\alpha_{\mathrm{ac}_i} = 0$ results in

$$\det\begin{bmatrix} \rho_t & \rho & 1 & 0 \\ u_t & a\cos\theta_{\mathrm{ac}_o} & 0 & -\sin\theta_{\mathrm{sh}} \\ v_t & a\sin\theta_{\mathrm{ac}_o} & 0 & \cos\theta_{\mathrm{sh}} \\ p_t & \rho a^2 & 0 & 0 \end{bmatrix} = 0 \tag{15}$$

The difficult part is the determination of the angles θ_{ac_o} and θ_{sh}. One possible assumption is that both angles are close enough to some dominant direction θ. After some simplifications, one gets

$$p_t - \rho a(u_t\cos\theta + v_t\sin\theta) = 0 \tag{16}$$

If it is assumed that $\theta = \theta^\star \approx \theta_{\mathrm{ac}_o}$, one will have the BC

$$(p - \rho a u^\star)_t = 0$$

which is similar to what was used intuitively in the earlier model. In fact, it is not obvious that this $\theta^\star$ direction should be selected, and probably is only a good choice for a wave close to boundary normal direction, where the reflected wave direction is close to the incidence one.

There is really no reason to assume the acoustic and shear perturbations are aligned. Therefore, $\theta_{\mathrm{ac}_o} \neq \theta_{\mathrm{sh}}$, and one may take $\tan\theta_v = -(u/v)$. However, this is only true for a steady shear wave. This is not a valid assumption here, because we are dealing with the transient part of the solution that is representing a moving shear layer.

To apply this model [Eq. (15)] to a practical problem we need more knowledge about the direction of the transient components of the outgoing acoustic and shear waves near the outer boundary.

V. Conclusions

The behavior of residual waves was studied, and two general tools to accelerate the convergence of numerical simulation of steady-state problems were introduced. First, soft wall BC was designed and optimized for a range of practical problems, and it was shown how gains of up to 50% in running time can be acheived. Its independence to grid size was demonstrated, and its limitations in problems involving shock waves were discussed. Then absorbing outer BCs were studied, and importance of angle of incidence in rate of convergence was shown. A method for numerical calculation of directions of incident and reflected waves was shown. Effective wave models for designing absorbing BCs should involve direction of different waves, but it was in practice hard to apply these directions. By slowing down the waves near the outer boundary, waves will arrive normal to the boundary, and because of less reflection, one can easily speed up this code.

Appendix: Wave Front Tracking

It proved difficult to visualize the path taken by the returning waves because these are weaker than the outgoing waves. Instead, a technique is used that provides information directly about the wave path. To study movement of the characteristic surfaces (see Acknowledgment) in a flowfield (governed by the Euler equations) one may use the parameterization

$$X(a, t): \mathbb{R}^2 \longrightarrow \mathbb{R}^2$$

of the surface at time t. Movement of these surfaces are described by

$$X_t^{\pm} = \boldsymbol{u}(X, t) \pm a\boldsymbol{n}(X)$$

for acoustic waves and

$$X_t^0 = \boldsymbol{u}(X, t)$$

for shear waves, where $\boldsymbol{n}(X)$ is the normal vector to the characteristic surface. One can describe all of these by one equation,

$$\phi_t - [\boldsymbol{u}\cdot\nabla\phi + \phi a|\nabla\phi|] = 0 \tag{A1}$$

where $\phi = \pm 1$ captures $X\pm$ and $\phi = 0$ captures the shear wave X^0. In fact, ϕ is constant on X surfaces. Other level contours have no physical meaning. For outgoing waves, one can write

$$\phi_t - \phi[\boldsymbol{u}\cdot\nabla\phi + a|\nabla\phi|] = 0 \tag{A2}$$

then all of the level contours show the outward propagating acoustic waves for different times.

For the center of a cell numbered (i, j), assume

$$\Delta_\xi^- = \frac{\phi_{i,j} - \phi_{i-1,j}}{\Delta\xi} \qquad \Delta_\xi^+ = \frac{\phi_{i+1,j} - \phi_{i,j}}{\Delta\xi}$$

$$\Delta_\eta^- = \frac{\phi_{i,j} - \phi_{i,j-1}}{\Delta\eta} \qquad \Delta_\eta^+ = \frac{\phi_{i,j+1} - \phi_{i,j}}{\Delta\eta}$$

To apply a sort of upwind scheme, one can write Eq. (A2) in the form

$$\phi_t - \phi[\boldsymbol{u} + a(\nabla\phi/|\nabla\phi|)]\cdot\nabla\phi = 0 \tag{A3}$$

where $\boldsymbol{n} = \nabla\phi/|\nabla\phi|$ is the unit normal to the characteristic surface. The value inside the bracket is the convection velocity for evolution of the scalar field ϕ. For the upwind method used in this work, the direction of $\boldsymbol{n}$ at each cell will suggest which value of $\Delta-$ or Δ^+ should be used. If (u, v) are the velocity components in, respectively, ξ and η directions, the discretized equation follows as

$$\frac{\phi_{ij}^{n+1} - \phi_{ij}^n}{\Delta t} = \phi_{ij}^n\left[(u\Delta_\xi + v\Delta_\eta) + a\sqrt{\Delta_\xi^2 + \Delta_\eta^2}\right] \tag{A4}$$

This scheme, although with a low order of accuracy, especially close to the outer boundary where the common practice is using coarse mesh, is always stable and provides enough accuracy for this qualitative study. Indeed we will show that some quantities are measured very accurately by this method.

A device due to Harabetian[7] is used here that allows reflected waves to be seen. He introduces two functions, ϕ_1 (for outgoing waves) and ϕ_2 (for incoming waves), both satisfying Eq. (A2) and sets

$$\phi_2 = \phi_1 \tag{A5}$$

on the outer boundary. Throughout the flow at $t = 0$, $\phi_1 = 1$ and $\phi_2 = 1$, but ϕ_1 is set to zero on the airfoil surface. This generates a wave front, lying on the surface of the airfoil at time $t = 0$, which propagates outward, and after hitting the outer boundary is reflected back toward the surface of the airfoil.

The level lines of ϕ follow acoustic wave fronts in a medium moving with velocity $\boldsymbol{u}(x, y)$ and having a sound speed $a(x, y)$. Equation (A2) can also be solved using local timesteps, to simulate wave behavior under local timestepping and using the values of $\boldsymbol{u}$ and a from the Euler solver. The simulated outgoing waves agreed well with those seen in the residual visualization of the Euler code used in this work.

For the same test case as in Sec. I.B, Fig. 20a shows the outgoing waves (ϕ_1) at a time that roughly corresponds to the Euler solution in Fig. 3b; the waves are found inside the region (★★). It shows the same pattern of a forward-moving shock. The waves that initially traveled downstream have already left the domain, creating reflected waves (ϕ_2) that move rapidly around the coarse mesh near the outer boundary and, not quite so quickly, along the line $y = 0$. The effect is that the returning waves envelop the airfoil in the sort of pattern that can be seen in Fig. 20b. Because of the fine mesh that usually surrounds any solid boundary, there is a tendency for the waves that arrive earliest to slow down and wait for the associated waves to catch up. This is the same mechanism by which waves arrive parallel to a beach. The returning waves, therefore, impact almost simultaneously on the airfoil. The moment at which this happens agrees closely with that at which the residuals in the Euler calculation are halted in their decline (i.e., the end of a bump in the conventional residual history in Fig. 2). At this moment, also, a fresh set of outgoing waves will be generated to renew the cycle.

This wave focusing is clearly the mechanism by which the residual history is tuned to a dominant frequency. There is satisfactory agreement between the period predicted from the eikonal computation and that observed in the Euler code, both of about 170 ± 5 iterations (see Figs. 2 and 20b).

Also the solution of the eikonal equation is used to predict the angles at which outgoing waves intersect the outer boundary. Figure 18 shows the angle between the wave normal ($\nabla\phi_1$) and the boundary curve, at the moment of reflection, as a function of the location on the outer boundary. From this figure can be seen that it is a very poor approximation to take this angle as 90 deg.

Acknowledgment

E. Harabetian is acknowledged for his 1990 private communication on capturing characteristic surfaces discussed in the Appendix.

References

[1]Mazaheri, K., "Numerical Wave Propagation and Steady State Solutions," Ph.D. Thesis, Dept. of Aerospace Engineering, Univ. of Michigan, Ann Arbor, MI, Oct. 1992.

[2]Roe, P. L., "Approximate Riemann Solvers, Parameter Vectors, and Difference Schemes," *Journal of Computational Physics*, Vol. 43, No. 2, 1981, pp. 357–372.

[3]Jameson, A., Schmidt, W., and Turkel, E., "Numerical Solutions of the Euler Equations by a Finite-Volume Method Using Runge–Kutta Time-Stepping Schemes," AIAA Paper 81-1259, 1981.

[4]Engquist, B., and Majda, A., "Absorbing Boundary Conditions for the Numerical Simulation of Waves," *Mathematics of Computation*, Vol. 31, No. 139, 1977, pp. 629–651.

[5]Bayliss, A., and Turkel, E., "Far Field Boundary Conditions for Compressible Flow," *Journal of Computational Physics*, Vol. 48, 1982, pp. 182–199.

[6]Roe, P. L., "Remote Boundary Conditions for Unsteady Multidimensional Aerodynamic Computations," *Computers and Fluids*, Vol. 17, No. 1, 1989, pp. 221–231.

[7]Harabetian, E., "Propagation of Singularities, Hamilton–Jacobi Equations, and Numerical Applications," *Transactions of American Mathematics Society* (submitted for publication).

D. S. McRae
Associate Editor